EES Batteries

PAPER

Published on 30 June 2026

Cite this: DOI: 10.1039/d6eb00128a

Controlled lithium stripping enables a stable interface for long-cycling anode-free solid-state batteries

Jiwei Wang, [a] Yuxuan Zhang, [b] James Torres, [b] Cheng Xu, [a] Mengting Ye,[a] Selim Halacoglu, [a] Xianhui Zhao, [c] Ercan Cakmak,[d] Michael Geiwitz, [e] Kenneth S. Burch [e] and Hongli Zhu *[a]

Anode-free solid-state batteries (AFSSBs) are a promising route toward achieving high energy density. In these cells, the anode contains no pre-stored lithium (Li). Instead, the entire Li inventory originates from the cathode and is freshly deposited onto a bare current collector during charging. However, achieving uniform and defect-free Li plating on this bare current collector remains a major challenge, often resulting in low Li plating/stripping efficiency and rapid capacity decay. Here, for the first time, *operando* neutron imaging is employed to visualize Li plating/stripping behavior in an anode-free full cell with $LiNi_{0.82}Mn_{0.07}Co_{0.11}O_2$ (NMC) as the cathode. *Operando* measurements reveal that complete stripping of Li leaves isolated Li residues on the current collector, which degrades the interfacial contact between the current collector and the solid-state electrolyte. To mitigate this interfacial issue and promote more uniform Li deposition, we implement a discharge-cutoff-voltage strategy that intentionally retains a thin residual Li layer after stripping. This preserved Li-containing interfacial reservoir not only improves interfacial contact but also serves as an *in situ* formed seed layer that enables more homogeneous subsequent Li plating. As a result, the optimized anode-free cell with limited stripping depth exhibits excellent long-term cycling stability, maintaining a discharge capacity of 112.1 mAh g^{-1} with a capacity retention of 80.6% and an average coulombic efficiency of approximately 99.9% after 500 cycles at 0.25 C. In contrast, the cell with a conventional discharge cutoff voltage of 2.8 V exhibits rapid capacity decay, retaining only 59.7 mAh g^{-1} after 50 cycles with a capacity retention of 40.7%. This work demonstrates that limiting deep stripping to preserve a thin Li-containing interfacial layer can effectively improve the cycling stability of sulfide-based AFSSBs.

Received 14th June 2026,
Accepted 29th June 2026

DOI: 10.1039/d6eb00128a

rsc.li/EESBatteries

Broader context

Advancing high-energy-density batteries is critical for electrification and renewable energy integration. Anode-free solid-state batteries offer a promising pathway but are limited by unstable lithium plating/stripping and interfacial degradation. A critical challenge arises from the inability to directly probe lithium behavior within buried solid–solid interfaces under operating conditions. This lack of mechanistic understanding obscures how lithium plating and stripping lead to contact loss and performance decay, thereby hindering the rational design of stable anode-free systems. Here, we reveal the dynamic evolution of lithium at the buried current collector interface during cycling and show that complete lithium stripping disrupts interfacial contact by leaving behind discontinuous inactive lithium. Guided by this insight, we demonstrate that regulating the discharge cutoff voltage to retain a thin interfacial lithium layer can mitigate contact loss and promote more stable subsequent deposition. This work highlights electrochemical regulation as a powerful strategy for interface design and provides a general framework for controlling metal deposition in solid-state and related electrochemical systems.

1. Introduction

All-solid-state batteries (ASSBs) are widely regarded as promising next-generation energy storage systems, owing to their combination of non-flammable solid-state electrolytes (SSEs) with high-specific-capacity lithium (Li) metal anodes.[1–4] Among various ASSB configurations, anode-free solid-state batteries (AFSSBs) are particularly attractive for maximizing specific energy density.[5,6] When coupled with a high-voltage

[a]*Department of Mechanical and Industrial Engineering, Northeastern University, 360 Huntington Avenue, Boston, Massachusetts 02115, USA. E-mail: h.zhu@neu.edu*
[b]*Neutron Scattering Division, Oak Ridge National Laboratory, Oak Ridge, Tennessee 37831, USA*
[c]*Environmental Sciences Division, Oak Ridge National Laboratory, Oak Ridge, Tennessee 37831, USA*
[d]*Materials Science and Technology Division, Oak Ridge National Laboratory, Oak Ridge, Tennessee 37831, USA*
[e]*Department of Physics, Boston College, Chestnut Hill, Massachusetts 02467, USA*

cathode such as $LiNi_{0.8}Mn_{0.1}Co_{0.1}O_2$, pack-level energy densities exceeding 400 Wh kg^{-1} are theoretically attainable due to the elimination of the pre-stored Li anode.[7,8] However, the Li-free feature that enables this advantage also makes the operation of AFSSBs challenging. Since all the active Li originates from the cathode and must be freshly deposited onto a bare current collector (CC) during charge, it imposes strict requirements on the reversibility of Li plating/stripping at the CC/SSE interface.[9,10] The intrinsic chemical and crystallographic mismatches between Li and the rigid CC often result in spatially nonuniform Li nucleation and growth, leading to void formation at the CC/SSE interface upon stripping.[11,12] Consequently, nonuniform Li morphology, loss of intimate CC/SSE contact, locally amplified current density, and a rapid increase in interfacial resistances are observed. Because the lithium reservoir in anode-free cells is intrinsically limited, even slight inefficiencies (the formation of 'dead' Li, incomplete stripping or Li entrapment within surface irregularities) can lead to rapid capacity degradation.[13,14] Therefore, achieving both high energy density and durable cycling in AFSSBs critically depends on controlling Li nucleation, achieving laterally uniform deposition, and preserving continuous mechanical/electrochemical contact throughout repeated plating and stripping processes.[15,16]

Despite extensive interfacial engineering efforts, including the use of stable interlayers[17–19] and surface modification of current collectors with lithophilic metal seeds,[20–25] the mechanistic origin of Li instability in AFSSBs remains poorly understood. These knowledge gaps stem from the difficulty in directly observing Li evolution within the solid–solid interface under realistic operating conditions. Conventional *ex situ* electron microscopy perturbs fragile Li morphologies and cannot capture the dynamic evolution within buried interfaces. X-ray imaging offers excellent spatial resolution but weak elemental contrast for Li and limited sensitivity to thin, laterally discontinuous Li layers sandwiched between dense components. *Operando* neutron imaging addresses these limitations in a complementary way. Lithium exhibits a strong neutron interaction contrast relative to typical SSEs, metallic current collectors, and NMC-type cathodes. As a result, neutron transmission can map Li with high sensitivity, enabling nondestructive visualization through thick cell walls under realistic electrochemical cycling conditions.[26] Time-resolved (*operando*) acquisition further enables direct correlation of spatial Li redistribution with the instantaneous current, voltage, and state of charge, elucidating how plated Li domains become isolated and how stripping progresses to generate discrete and interfacial voids.

Herein, *operando* neutron imaging was employed to directly visualize the dynamic evolution of Li during plating/stripping processes in a sulfide-based anode-free full cell. *Operando* neutron imaging reveals that complete stripping of Li leaves isolated Li residues on the current collector, which degrades interfacial contact between the current collector and the solid-state electrolyte. Guided by these *operando* insights, a simple yet effective interfacial-regulation strategy is proposed in this work using a discharge-cutoff-voltage protocol that intentionally retains a thin residual Li layer on the current collector after stripping. Limiting the discharge depth preserves a thin residual Li layer that provides abundant and uniformly distributed nucleation sites for subsequent Li deposition, while maintaining mechanical conformity and intimate contact that reduces local contact resistance. Practically, this approach reduces local current hot spots, suppresses void formation, and leads to a homogeneous morphology with uniform Li deposition. Because retaining residual Li reduces immediate energy output, the discharge cutoff voltage must be carefully optimized: insufficient retention fails to prevent contact loss, whereas excessive retention compromises energy density. In this study, we identify the minimal retained Li that preserves interfacial continuity, thereby extending the cycle life, improving coulombic efficiency (CE), and stabilizing capacity without forfeiting the core energy-density advantage of the anode-free design.

2. Results and discussion

To investigate the root of the poor efficiency of anode-free solid-state batteries, *operando* neutron imaging was employed to directly track the dynamic evolution of Li during plating and stripping processes in sulfide-based AFSSBs coupled with an NMC cathode (Fig. 1a). Fig. S1 shows the 2D neutron transmission image of the AFSSBs before electrochemical cycling. To enhance the visibility of changes in the Li content during charge/discharge, the neutron transmission in all images was normalized by dividing the transmission in the pristine state to obtain the transmission change ratio, Tr_t/Tr_0, where Tr_t denotes the real-time neutron transmission intensity during cycling and Tr_0 represents the neutron transmission intensity in the pristine state.[27] Fig. S2 presents the voltage profile of the *operando* AFSSBs and the corresponding real-time evolution of Tr_t/Tr_0. In the *operando* images, the horizontal axis and vertical axis represent the spatial position within the cell and the cycling time, respectively. Pseudo-color mapping was used to represent the values of Tr_t/Tr_0 in the *operando* neutron images. Green regions with $Tr_t/Tr_0 = 1$ indicate a constant Li concentration, while color shifts toward blue ($Tr_t/Tr_0 > 1$) indicate a decrease in Li and shifts toward red ($Tr_t/Tr_0 < 1$) indicate an increase in Li. The colors at the anode side gradually changed to red during the charging process, reaching peak intensity at the end of the charge process. During discharge, the red color at the anode side gradually diminished with a light orange-yellow color remaining at the end of discharge, suggesting that a small amount of Li remained on the CC at the end of discharge.

Fig. 1b and c present detailed pseudo-color 2D images of the *operando* AFSSBs at specific state of charge (SOC) and depth of discharge (DOD). The pseudo-color 2D images display the behaviors of the whole *operando* cell, where the horizontal axis is the diameter of the cell and the vertical axis represents the position of the cell. As shown in Fig. 1b, with

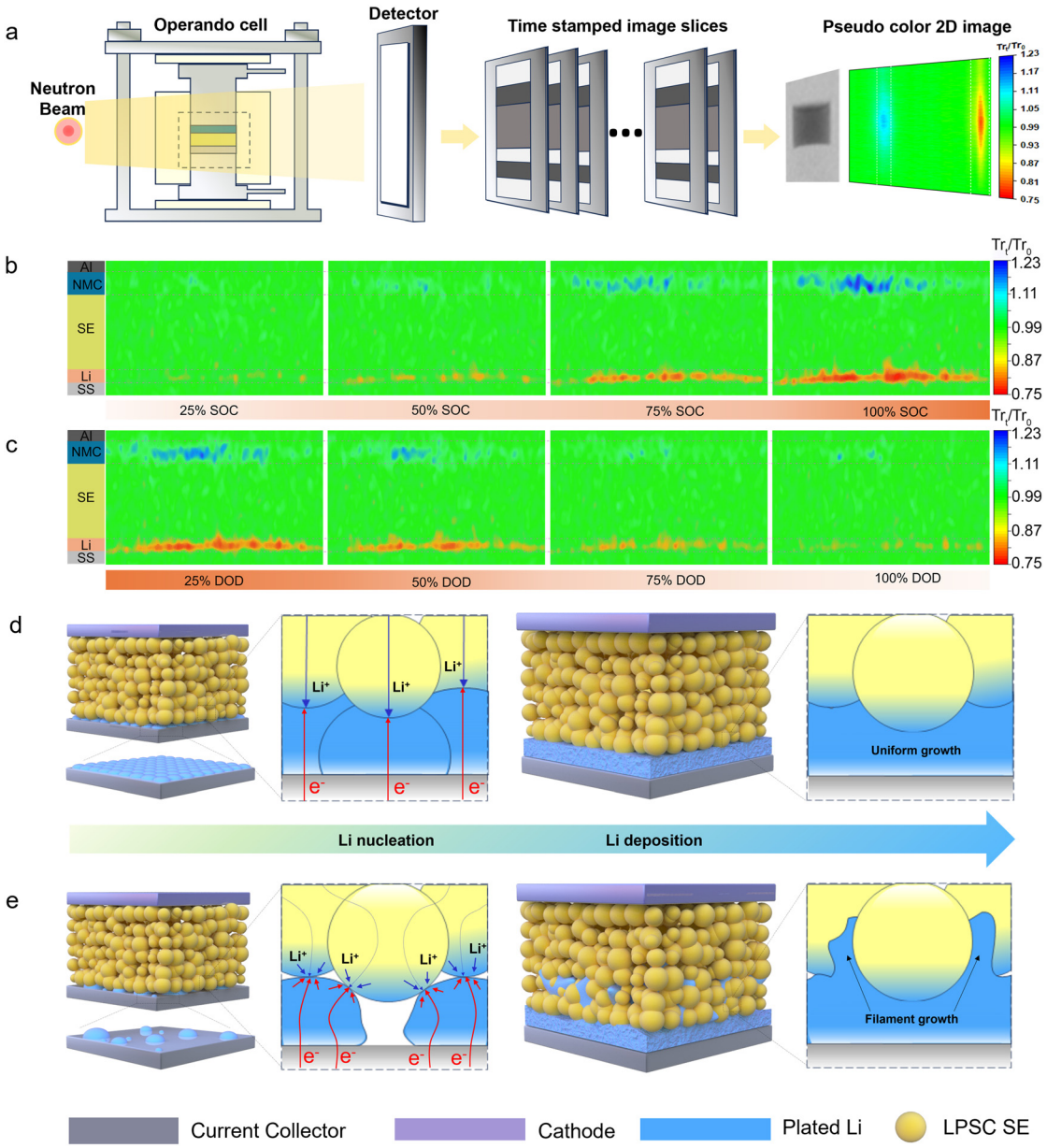

Fig. 1 (a) Schematic illustration of the *operando* neutron imaging studies of sulfide-based AFSSBs. Pseudo color 2D images of the *operando* cell at different (b) states of charge (SOC) and (c) depths of discharge (DOD). Schematic illustration of the effect of (d) controlled depth of stripping and (e) fully stripping on the subsequent Li nucleation and growth in sulfide-based AFSSBs.

SOC increasing, the color at the NMC cathode layer gradually turned blue and the color at the stainless-steel (SS) CC side gradually turned red, indicating that Li was extracted from the NMC cathode and plated onto the SS CC during the charging process. The noncontinuous red color observed at 25% SOC and 50% SOC suggests heterogeneous Li plating on the SS CC. As charging continues, the Li layer grows thicker, as indicated by a more intense red color at 100% SOC compared to that at 50% SOC. During the discharge process, the red color at the SS side gradually fades, suggesting that Li is stripped back toward the cathode (Fig. 1c). Notably, the initially continuous red color at 25% DOD evolves into a noncontinuous pattern, and at 100% DOD only a faint and discontinuous red contrast remains. This faint and discontinuous red contrast indicates the presence of a small amount of isolated and non-uniformly distributed residual Li on the SS current collector after stripping. Such a non-uniform residual Li morphology is likely to compromise interfacial stability during subsequent plating/stripping cycles.

Guided by insights from *operando* neutron imaging, we propose a facile and practical interfacial engineering strategy to stabilize the anode interface in AFSSBs by controlling the stripping depth of the electrochemically deposited Li reservoir during discharge (Fig. 1d). By tuning the discharge cutoff

voltage, a thin electrochemical Li residue remains on the current collector after stripping, which ensures intimate interfacial contact at the SE/CC interface. Additionally, the remaining thin electrochemical Li serves as an *in situ* formed seed layer that can promote uniform Li deposition in the subsequent replating cycle. In contrast, complete stripping of the electrochemically deposited Li leads to the formation of isolated, electrochemically inactive Li on the CC and interfacial voids at the SE/CC interface (Fig. 1e), resulting in nonuniform Li deposition in the subsequent cycles and accelerated capacity degradation in long-term cycling. To demonstrate the effects of the preservation of a continuous residual Li layer on the electrochemical performance, anode-free solid-state full cells paired with a $LiNbO_3$-coated $LiNi_{0.82}Mn_{0.07}Co_{0.11}O_2$ (LNO@NMC) cathode were assembled and evaluated. The cathode composite consisted of LNO@NMC, $Li_{5.4}PS_{4.4}Cl_{1.6}$ (LPSC), and vapor grown carbon fiber (VGCF) in a weight ratio of 75 : 24 : 1. Bare SS was used as the anode current collector for Li plating/stripping. Fig. S3 shows the electrochemical performance of AFSSBs discharged to different cutoff voltages at a rate of 0.1 C. As shown in Fig. S3a, the initial charge–discharge profiles of the cells discharged to 2.8, 3.2, and 3.5 V overlapped well, indicating similar electrochemical behaviors within the three cells. Increasing the discharge cutoff voltage leads to a gradual decrease in discharge capacity because a larger amount of Li is intentionally retained on the CC after stripping. Despite this capacity sacrifice, a remarkable improvement in cycling stability is observed (Fig. S3b). The cells discharged to 2.8 and 3.2 V undergo rapid capacity decay, whereas the cells discharged to 3.5 V show significantly improved cycling stability, with around 70.1% capacity retention after 50 cycles, while the cell with 2.8 V cutoff exhibits a capacity retention of 11.4% after 50 cycles. Meanwhile, the average CE improves from 95.2% for the 2.8 V cutoff cell to 99.5% for the 3.5 V cutoff cell, indicating substantially improved reversibility of Li plating/stripping. The improved cycling stability and CE suggest that controlling the stripping degree effectively suppresses the interfacial degradation associated with deep Li depletion. By retaining a thin residual Li layer on the CC, the interfacial continuity can be preserved, thereby mitigating contact loss at the CC/SE interface and providing more homogeneous deposition sites for subsequent Li plating. The *ex situ* electrochemical impedance spectroscopy (EIS) spectra of the cells after they are discharged to different discharge cutoff voltages reveal that the interfacial resistance of the cell decreases with increasing discharge cutoff voltage (Fig. S4). The reduced interfacial resistance indicates improved interfacial contact. Top-view scanning electron microscopy (SEM) showed that isolated Li covered the SS CC at a discharge cutoff voltage of 2.8 V, whereas uniform Li coverage on the SS CC was observed at a discharge cutoff voltage of 3.5 V (Fig. S5). This uniform Li residual layer not only maintains intimate interfacial contact but also acts as a seed layer that can provide abundant and uniformly distributed nucleation sites for subsequent Li deposition, thus promoting uniform Li deposition and enhancing long-term cycling performance.

To further evaluate the effect of the Li seed layer induced by discharge voltage control on cycling performance, electrochemical tests were conducted using an LPSC solid electrolyte with an optimized microstructure *via* mechanical ball-milling. Previous studies have demonstrated that mechanically milled LPSC powders with reduced particle size can enhance electrochemical stability by refining the grain structure and improving interfacial contact.[28] The anode-free full cells were assembled by pairing with a $LiNbO_3$-coated $LiNi_{0.82}Mn_{0.07}Co_{0.11}O_2$ (LNO@NMC) cathode, in which the cathode composites were composed of LNO@NMC : SE : vapor grown carbon fiber (VGCF) in a weight ratio of 70 : 28.5 : 1.5. To further improve the overall electrochemical performance, Ag-coated SS foils (Ag@SS) were used as the current collector to promote the initial Li plating uniformity in the optimized cell configuration. The electrochemical performance of the anode-free cells was initially evaluated using the cathode with an areal capacity of 1.78 mAh cm^{-2}. Fig. 2a compares the electrochemical cycling performance of the anode-free cells with discharge voltages of 2.8 V and 3.5 V, at a rate of 0.1 C (equivalent to 0.178 mA cm^{-2}). Although the cell discharged to 2.8 V exhibited a slightly higher discharge capacity in the early cycles compared to the one discharged to 3.5 V, its capacity began to decline rapidly thereafter. By the 50^{th} cycle, its capacity was significantly lower than that of the cell discharged to 3.5 V, indicating inferior long-term cycling stability under this discharge condition. Fig. 2b and c show the galvanostatic charge–discharge profiles of the two cells at the 1^{st} cycle and 50^{th} cycle, respectively. The cell with a discharge voltage of 2.8 V exhibits initial charge and discharge capacities of 215.2 and 173.6 mAh g^{-1}, respectively, corresponding to an initial CE of 80.7%. In contrast, the cell with a discharge voltage of 3.5 V displays capacities of 217.8 and 167.3 mAh g^{-1}, corresponding to an initial CE of 76.8%. It should be noted that the charge capacities of the two cells are almost the same and around 2 mAh g^{-1} variation is normal in solid-state batteries. In the cell with a discharge voltage of 2.8 V, the discharge capacity at 3.5 V is 164.5 mAh g^{-1}, thus the CE difference between 2.8 V and 3.5 V is around 4%. Therefore, the effective capacity difference between the 2.8 V and 3.5 V cutoff cells is only ~9 mAh g^{-1}, corresponding to ~4% of the charge capacity. Considering that the average discharge voltages of the two cells are nearly identical, the corresponding electrode-level energy-density reduction is estimated to be only ~5.2%, indicating that a substantial improvement in cycling stability is achieved with a relatively small energy-density penalty. This remaining 9 mAh g^{-1} (equivalent to 0.083 mAh cm^{-2}) Li can function as the Li seeds for the Li plating in the subsequent cycles. As a result, the cell with a cutoff voltage of 3.5 V shows a discharge capacity of 131 mAh g^{-1} after 50 cycles, yielding a capacity retention of 80%, whereas the cell with a cutoff voltage of 2.8 V delivers a discharge capacity of around 79 mAh g^{-1} after 50 cycles with a capacity retention of 45.5%. Moreover, the discharge voltage curve displays a pronounced linear drop from 3.6 V to 2.8 V, indicating interfacial contact loss at the CC/SE interface, likely resulting in the formation of dead Li due to

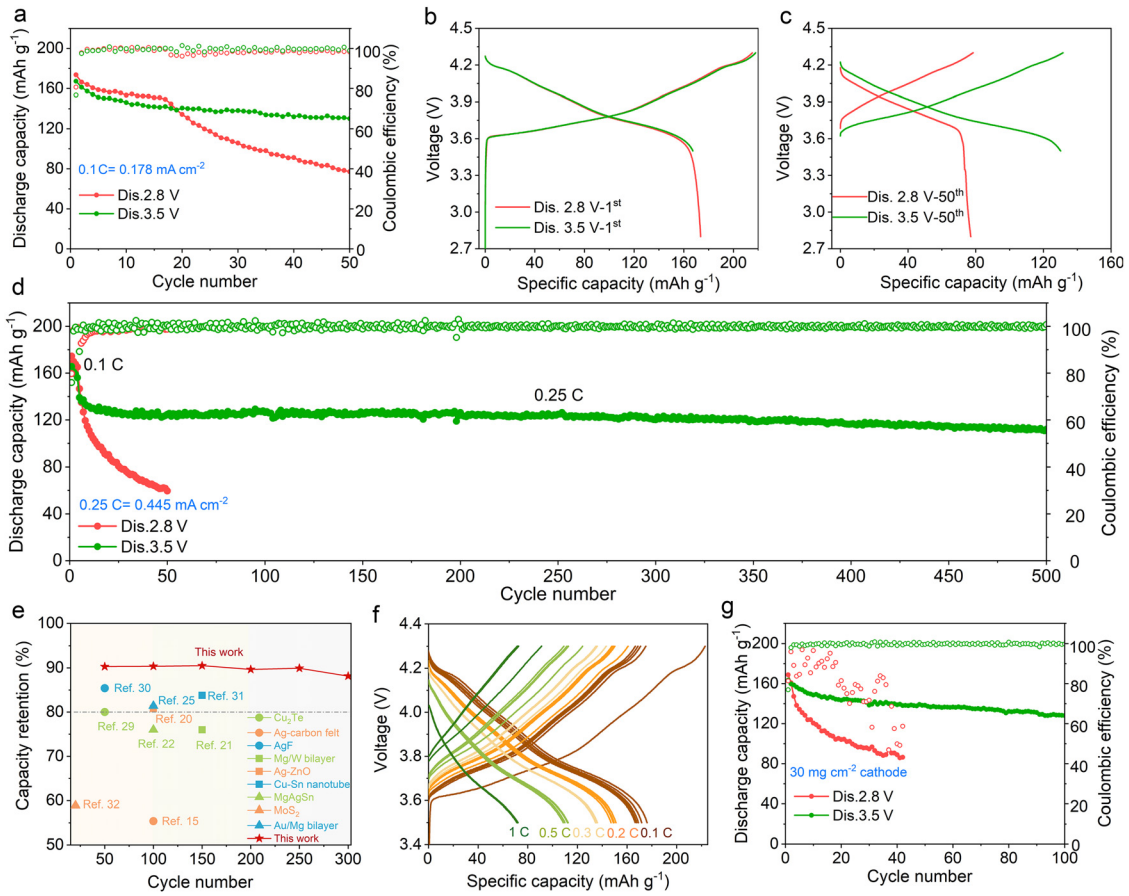

Fig. 2 (a) Long-term cycling performances and coulombic efficiencies of AFSSBs at 0.1 C (10 mg cm^{-2}, 0.178 mA cm^{-2}) with discharge cutoff voltages of 2.8 V and 3.5 V, respectively. Comparison of galvanostatic charge–discharge curves of (b) the 1st cycle and (c) the 50th cycle for the cells with 2.8 V and 3.5 V discharge cutoff voltages. (d) Long-term cycling performances and coulombic efficiencies of AFSSBs at 0.25 C (0.445 mA cm^{-2}) with discharge cutoff voltages of 2.8 V and 3.5 V, respectively. (e) Comparison of the full cell performance of this work with previously reported sulfide-based AFSSBs. (f) Galvanostatic charge–discharge curves of AFSSBs with a discharge cutoff voltage of 3.5 V at different current rates. (g) Long-term cycling performances and coulombic efficiencies of AFSSBs at 0.1 C (30 mg cm^{-2}, 0.534 mA cm^{-2}) with discharge cutoff voltages of 2.8 V and 3.5 V, respectively. The cathode mass loading is 30 mg cm^{-2} for both cells.

the electronically disconnected regions at the interface. Compared with the bare SS (Fig. S3b), Ag@SS improves the cycling stability of the cell discharged to 2.8 V, enabling relatively stable cycling during the initial 17 cycles. This result suggests that the optimized current collector can partially alleviate the interfacial instability during the early stages of cycling. However, rapid capacity decay is subsequently observed upon prolonged cycling, indicating that repeated deep Li stripping continuously deteriorates the anode interface and eventually leads to severe interfacial degradation. In contrast, the cells discharged to 3.5 V exhibit significantly improved cycling stability for both bare SS and Ag@SS current collectors. These results suggest that, although current collector engineering can improve the initial cycling behavior, the long-term stability of AFSSBs is predominantly governed by the extent of Li stripping. By intentionally preserving a thin residual Li layer after discharge, interfacial continuity can be maintained, thereby mitigating contact loss and suppressing the progressive interfacial degradation associated with complete Li depletion. As a result, more stable and homogeneous Li plating/stripping can be achieved during extended cycling, leading to substantially improved electrochemical reversibility and cycling stability. To verify the uniformity of the retained Li at the discharge cutoff voltage of 3.5 V, SEM images were recorded to examine the surface of the CC after initial discharge at cutoff voltages of 2.8 V and 3.5 V, respectively. As shown in Fig. S6, the CC surface after discharging to 2.8 V exhibits a highly nonuniform Li distribution, with localized Li accumulation and large Li-deficient regions, indicating heterogeneous Li stripping behavior and interfacial nonuniformity. In contrast, discharging to 3.5 V results in a more homogeneous Li distribution across the CC surface, where Li is evenly distributed without obvious localized accumulation. The uniformly retained Li at a 3.5 V cutoff is expected to reduce interfacial heterogeneity and promote more reversible Li plating/stripping in subsequent cycles.

To further investigate the effect of discharge cutoff voltage on the cycling performance of anode-free solid cells, the two

cells were galvanostatically cycled at an increased current density of 0.25 C (equivalent to 0.445 mA cm^{-2}). Prior to the long-term cycling, four initial formation cycles were carried out at a low current rate of 0.1 C to ensure interfacial stabilization (Fig. 2d). From the galvanostatic charge–discharge voltage profiles, both cells exhibited a slower capacity decrease in the four initial formation cycles. However, the cell discharged to 2.8 V showed a fast capacity degradation at 0.25 C, and it only exhibited a discharge capacity of around 59.7 mAh g^{-1} after 50 cycles (Fig. S7), corresponding to a capacity retention of 40.7% (calculated based on the discharge capacity of 146.7 mAh g^{-1} at the 5^{th} cycle). In contrast, the cell discharged to 3.5 V displayed an excellent long-term cycling stability with a discharge capacity of 121 mAh g^{-1} after 300 cycles (Fig. S8) and 112.1 mAh g^{-1} after 500 cycles, yielding a superior capacity retention of 80.6% after 500 cycles (calculated based on the discharge capacity of 139.1 mAh g^{-1} at the 5^{th} cycle). Moreover, the average CE of the 3.5 V cell remained more stable and closer to 99.9% throughout cycling, while that of the 2.8 V cell showed a lower value of 98.1% with a gradual decline. Fig. 2e and Table S1 present a comparison of the full cell performance of this work with previously reported sulfide-based AFSSBs.[15,20–22,25,29–32] As highlighted by the red-star curve, our cell delivers markedly improved cycling stability and capacity retention under practical cycling conditions, underscoring the potential of this approach for realizing high-energy-density AFSSBs.

Fig. S9 compares the rate performance of the two anode-free solid cells, which were tested at C-rates ranging from 0.1 C to 1 C, with five cycles performed at each rate. For the cell with a discharge cutoff voltage of 2.8 V, pronounced voltage fluctuations and short-circuiting appeared during the fifth cycle at 0.3 C, and these instabilities became more severe at higher rates of 0.5 C and 1 C (Fig. S10). The failure is mainly because, at a high current rate, Li is deposited under increased local current density, which can promote non-uniform deposition and exacerbate interfacial heterogeneity. Meanwhile, deep Li stripping at 2.8 V induces interfacial void formation and loss of interfacial contact. Their combination can result in localized current concentration during subsequent Li deposition, leading to a short circuit. In contrast, the cell with a discharge cutoff voltage of 3.5 V exhibited stable cycling up to 1 C without short-circuiting, delivering a discharge capacity of around 110 mAh g^{-1} at 0.5 C and 80 mAh g^{-1} at 1 C (Fig. 2f). This improved rate performance indicates that the *in situ* formed Li seed layer can promote uniform Li deposition and stripping. Fig. S11 further compares the long-term cycling performance of the two cells at a high rate of 1 C. It shows that the cell with a discharge cutoff voltage of 2.8 V exhibits rapid failure and short-circuiting, indicating severe interfacial degradation and uneven Li plating at high rates. In contrast, the cell discharged to 3.5 V demonstrates stable cycling for over 350 cycles without short-circuiting.

The electrochemical performance of the two anode-free cells was further evaluated under a high cathode mass loading of 30 mg cm^{-2} (Fig. 2g). Despite the increased mass loading, both cells exhibited comparable initial discharge capacities of 168.9 and 163.5 mAh g^{-1}, with initial CEs of 81.3% and 76.9%, respectively. However, the cell discharged to 2.8 V experienced accelerated capacity degradation (Fig. S12), whereas the cell discharged to 3.5 V retained 78.3% of its capacity after 100 cycles. Moreover, the average CE of the 3.5 V cell remained above 99.5% throughout cycling, indicating a stable anode interface. In contrast, the CE of the 2.8 V cell exhibited significant fluctuations and dropped below 80% after only 15 cycles, reflecting severe interfacial degradation under high areal capacity conditions.

To study the underlying mechanisms of the "Li seed layer" induced by the discharge voltage control on subsequent Li plating/stripping behavior, *in situ* EIS and distribution of relaxation time (DRT) were carried out to monitor the resistance evolution in the solid-state anode-free full cells cycled with discharge cutoff voltages of 2.8 V and 3.5 V during the initial three cycles. The DRT technique, which converts EIS spectra into a distribution of relaxation time constant, enables the deconvolution of highly overlapping electrochemical processes in the complex AFSSB system and provides more precise identification of resistance contributions that are challenging to separate using conventional equivalent circuit modeling. The galvanostatic charge–discharge cycling of the cells with discharge cutoff voltages of 2.8 V and 3.5 V was performed in a mode with one hour charge/discharge steps followed by 30-min rest periods for EIS measurement at the 1^{st} and 3^{rd} cycles (Fig. S13). Fig. 3a displays the impedance evolution of the cell discharged to 3.5 V during the first cycle. During the charge process, the *in situ* EIS spectra show a large semicircle after the first one-hour charging, indicating high interfacial resistance at the onset of Li plating. The semicircular resistance exhibits a gradual shrinking and then increases again as charging continues. In contrast, the semicircular resistance during discharge displays a very small variation until the end of discharge at 3.5 V. The impedance evolution of the cell discharged to 2.8 V during the first charge process exhibits a similar trend to the cell discharged to 3.5 V (Fig. 3c). However, during the discharge process, the cell discharged to 2.8 V exhibits a more rapid and pronounced increase in interfacial impedance during the end stage of discharge compared to the cell discharged to 3.5 V. This suggests that complete stripping of the plated Li in AFSSBs can lead to an interface degradation issue.[33,34]

DRT contour two-dimensional (2D) images were derived from the *in situ* EIS to further diagnose the resistance differences between the two cells. In the DRT plots, R1 (10^{-6} to 10^{-5} s) primarily corresponds to ohmic resistances, including electronic contact resistances at current collectors and ionic conduction through the electrolyte, R2 (10^{-5} to 10^{-2} s) represents solid electrolyte interphase (SEI) formation and Li ion transport through the interfacial SEI layer, and R3 (10^{-2} to 10 s) corresponds to charge transfer and resistance at relaxation times above 10 s associated with mass transport and ion diffusion within the bulk materials.[15,35] From DRT images, both cells show a prominent R3 peak at the early stage of the

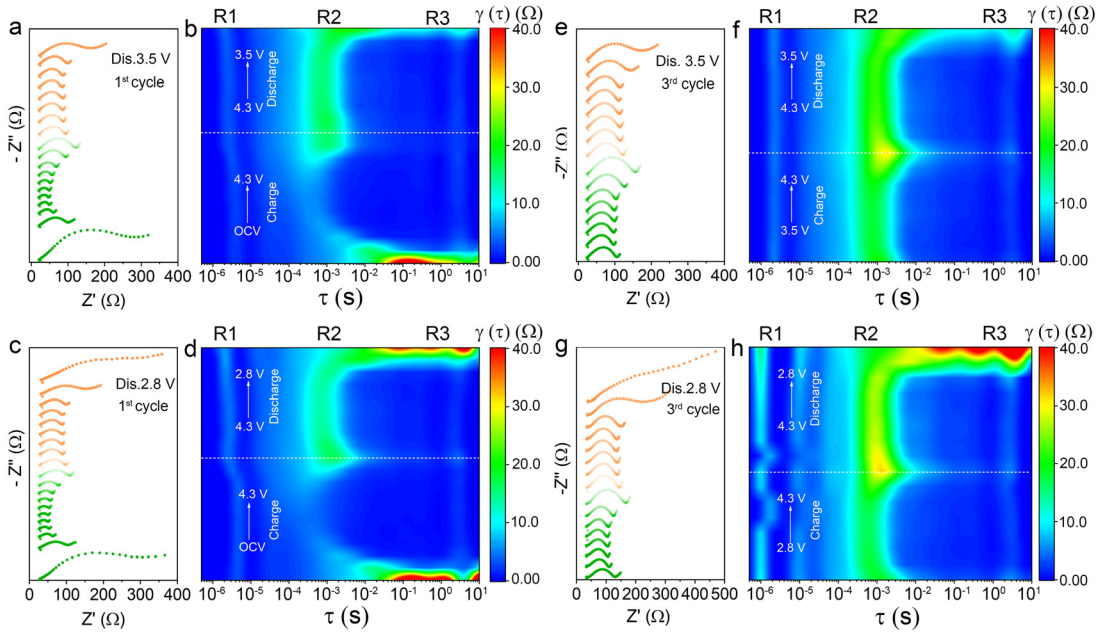

Fig. 3 *In situ* EIS plots of cells with discharge cutoff voltages of (a and e) 3.5 V and (c and g) 2.8 V at the 1st and 3rd cycles. DRT contour plots of the cells with discharge cutoff voltages of (b and f) 3.5 V and (d and h) 2.8 V at the 1st and 3rd cycles.

charging process in the first cycle (Fig. 3b and d). This high R3 can be attributed to the isolated and discontinuous Li nuclei formed on the current collector at the early stage, leading to poor electronic and ionic connectivity at the Li/SE interface. Although the resistance evolution during the 1st cycle charge appears comparable between the two cells in DRT contour images, the cell discharged to 2.8 V displays higher R1 and R3 at the end of discharge compared with the cell discharged to 3.5 V, indicating poor interfacial contact and sluggish charge transfer under deeper discharge conditions (Fig. S14). In the 3rd cycle, the resistance differences become significantly more pronounced (Fig. 3e and g). Both R1 and R3 remain relatively stable for the cell discharged to 3.5 V compared to those in the 1st cycle (Fig. 3f), suggesting a stable interface and uniform Li plating/stripping. In contrast, the cell discharged to 2.8 V shows a dramatic increase in both R1 and R3 at the 3rd cycle (Fig. 3h). The elevated R1 indicates worsening interfacial contact and non-uniform Li plating, possibly due to void formation at the CC/SE interface. Meanwhile, the significant growth in R3 reflects increased charge-transfer resistance, suggesting the accumulation of inactive Li and deteriorated interfacial kinetics. These results demonstrate that the 3.5 V cell maintains a more stable interface across cycles. This is likely because residual Li remaining after the 3.5 V discharge acts as a uniform seed layer for subsequent replating, which induces homogeneous Li deposition, thereby enhancing interfacial contact and promoting charge transfer kinetics through improved electronic and ionic percolation across the interface.

The influence of the remaining thin Li layer on electrochemical performance was further examined by micro-computed X-ray tomography (μ-CT). The anode-free cells for μ-CT measurements were cycled at 0.1 C with a cathode mass loading of around 30 mg cm^{-2}. Fig. 4a and b display reconstructed image slices of anode-free full cells after five cycles with discharge cutoff voltages of 3.5 V and 2.8 V, respectively. Fig. 4c and d present magnified views of the anode interface, while image segmentation was applied to extract the CC/Li and Li/SE interfaces. Three-dimensional (3D) renderings of the CC, Li, and SE phases from a sub-volume with an edge length of 330 μm are shown in Fig. 4e and f. For the cell cycled with a 2.8 V cutoff, isolated and nonuniform Li deposits were observed across the CC surface. These discontinuous, inactive Li regions caused poor interfacial contact and promoted void formation at the CC/SE interface, leading to rapid capacity decay. In contrast, the cell cycled with a 3.5 V cutoff retained a thin yet more uniform Li layer across the CC surface, indicating more homogeneous Li plating/stripping and intimate CC/SE interfacial contact.

Fig. 4g and h schematically illustrate the mechanistic role of residual Li after controlled stripping in governing subsequent Li plating behavior. During the complete stripping process, isolated inactive Li persists on the CC and interfacial voids are generated at the CC/SE interface, which induces heterogeneous nucleation and nonuniform Li growth during the subsequent plating. This nonuniform Li growth accelerates interfacial degradation during the subsequent stripping process, leading to increased void growth and dendrite formation with continued cycling. By contrast, when a thin residual Li layer is intentionally preserved through controlled discharge, it not only maintains an intimate interfacial contact but also functions as a seed layer that provides abundant and uniformly distributed nucleation sites for subsequent Li depo-

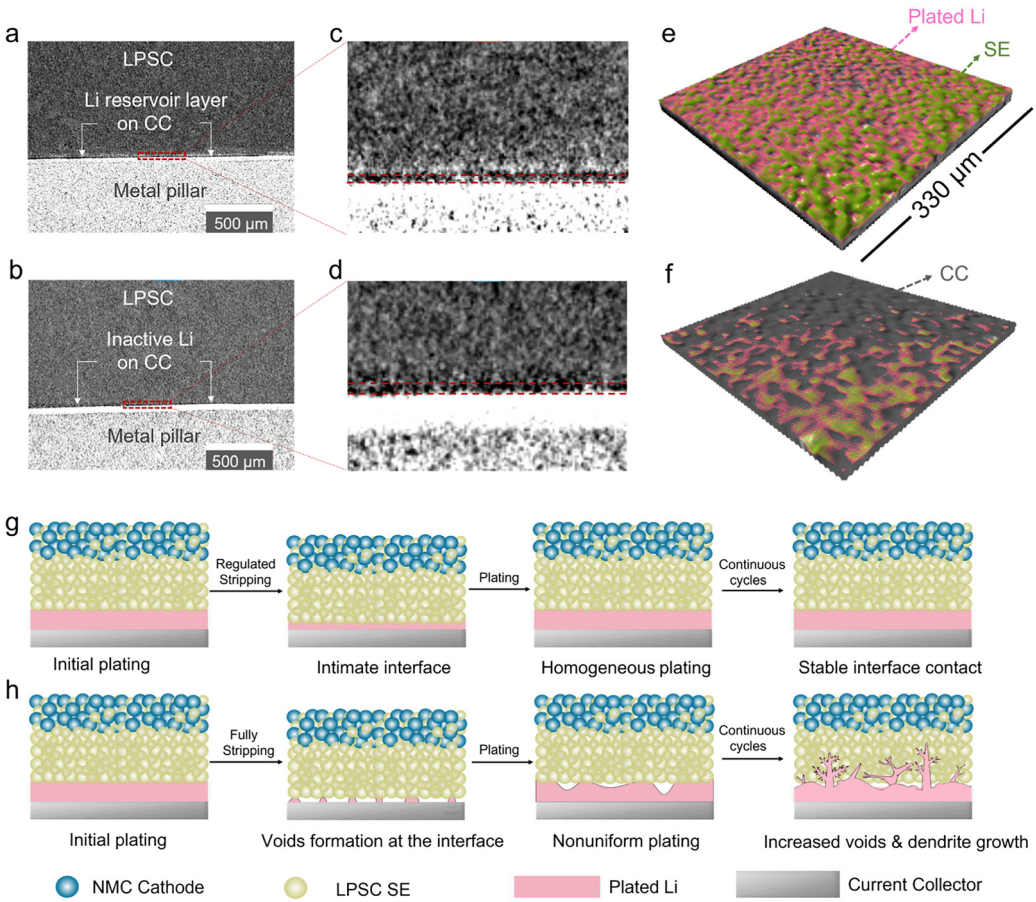

Fig. 4 Micro-computed X-ray tomography characterization of the anode–SE interfaces after 5 cycles. Reconstructed image slice from a scan of anode-free full cells with discharge cutoff voltages of (a) 3.5 V and (b) 2.8 V after 5 cycles at 0.1 C. The white layer is the stainless-steel current collector. (c) and (d) Magnified views of the anode interface in (a) and (b). 3D rendering of a sub volume at the anode interface for the cells with discharge cutoff voltages of (e) 3.5 V and (f) 2.8 V. Schematic illustration of the mechanistic impact of (g) the presence of a uniform Li seed layer and (h) the absence of a uniform Li seed layer on Li plating behaviors and long cycling stability in AFSSBs.

sition, thereby facilitating more homogeneous Li growth and improving interfacial stability during repeated cycles. Moreover, it suppresses the formation of voids and inactive Li at the interface in the subsequent stripping. Consequently, the presence of a retained thin Li layer mitigates interfacial degradation and suppresses the accumulation of isolated inactive Li, thereby enabling highly reversible plating/stripping and markedly extending the cycling stability of AFSSBs.

3. Conclusions

In anode-free solid-state batteries, all active Li is freshly supplied from the cathode and must nucleate and grow directly on a stainless-steel current collector, which is an intrinsically challenging setting for uniform deposition. *Operando* neutron imaging reveals that complete stripping fragments the plated Li into isolated, inactive domains and induces interfacial voids, resulting in contact loss and heterogeneous current distribution at the CC/SE interface. Guided by these mechanistic insights, a straightforward discharge-voltage-control protocol that intentionally retains a thin residual Li reservoir layer is shown to preserve conformal contact at the interface and promote uniform Li plating in the subsequent cycle. Corroborated by *in situ* EIS/DRT and μ-CT, this strategy suppresses void formation, lowers interfacial/charge-transfer resistance, and significantly improves cycling stability. Notably, similar discharge-cutoff-dependent improvements were observed for both bare SS and Ag-coated SS current collectors, confirming that the beneficial effect originates from controlled Li stripping and residual Li preservation rather than the specific current collector configuration. Under an optimized cell configuration with Ag@SS CC, the cell delivers a discharge capacity of 112.1 mAh g^{-1} with 80.6% capacity retention after 500 cycles at 0.25 C and an average CE of around 99.9%, whereas deeper stripping (2.8 V cutoff) triggers rapid fade and unstable efficiencies. Beyond providing a practical strategy to mitigate Li depletion and interfacial contact loss in sulfide-based AFSSBs, this work demonstrates how *operando* neutron imaging can provide mechanistic insights for future interface engineering. While the optimal discharge cutoff voltage is expected to depend on multiple factors, including the current collector pro-

perties, interlayer chemistry, cathode loading, cathode voltage profile, and solid electrolyte properties, preserving a Li-containing interfacial reservoir through controlled stripping represents a promising strategy for improving the reversibility and cycling stability of anode-free solid-state batteries.

4. Experimental section

4.1 Materials preparation

$Li_{5.4}PS_{4.4}Cl_{1.6}$ (LPSC) was synthesized *via* a mechanical ball-milling process followed by annealing.[36] Specifically, lithium sulfide (Li_2S, 99.98%, Sigma-Aldrich), phosphorus pentasulfide (P_2S_5, 99%, Sigma-Aldrich), and lithium chloride (LiCl, >99.98%, Sigma-Aldrich) were stoichiometrically mixed manually in an agate motor. The mixed powders were then transferred to a stainless-steel jar in an Ar glovebox and ball-milled at 500 rpm for 40 cycles, with each cycle consisting of 15 min of milling followed by a 15 min rest. After ball-milling, the mixture was sealed in a glass tube under vacuum and annealed at 510 °C for 2 h with a heating rate of 5 °C min^{-1}. To obtain fine LPSC, the as-prepared LPSC SE was subjected to a secondary ball-milling step. Specifically, 2 g of LPSC was placed into a zirconia jar with 2.5 mL of anhydrous toluene, and the ball-milling jar was sealed inside the glovebox. Ball milling was then conducted at a speed of 300 rpm for 16 h, using a cycle of 20 min of milling and a 5 min rest. Finally, the fine LPSC powders were obtained after vacuum drying the ball-milled powders in the glovebox chamber for 10 h.

4.2 Anode-free cell fabrication

The composite cathode was prepared by hand mixing the $LiNbO_3$-coated NMC cathode (MSE Supplies), fine LPSC, and vapor-growth carbon fibers at a weight ratio of 70 : 28.5 : 1.5. Anode-free full cells were fabricated by first compressing 80 mg of fine LPSC powder to a pellet at a low pressure of 40 MPa in a polyether ether ketone (PEEK) cell with a diameter of 10 mm. The cathode composites were then loaded on one side of the SE pellet and compressed with a 10 mm diameter steel pillar by hand. The cell stack was then pressed at a high pressure of 400 MPa for 1 min to densify the two layers. Afterwards, a 10-mm diameter metal foil disc (100 nm Ag-coated stainless steel (SS)) was placed on the other side of the SE pellet. The cell was then positioned in a SS frame and an external pressure of 15 MPa was applied by using a torque wrench during the cell testing. For the control cells employing bare SS current collectors, as-prepared LPSC without secondary ball-milling was used as the SE and the cathode composite consisted of $LiNbO_3$-coated NMC, fine LPSC, and vapor-growth carbon fibers at a weight ratio of 75 : 24 : 1. All other fabrication parameters were identical to those of the cell employing Ag-coated SS current collectors.

4.3 Electrochemical characterization

Electrochemical cycling measurements were conducted inside the Ar-filled glovebox to avoid air exposure. The electrochemical performance of the anode-free full cells was tested within the voltage range of 2.8–4.3 V *versus* Li^+/Li. *Operando* electrochemical impedance spectroscopy (EIS) measurement was carried out over a frequency range from 1 MHz to 10 mHz with an AC amplitude of 20 mV using a Biologic SP 150 potentiostat. Cells were galvanostatically cycled at a C rate of C/10. EIS spectra were collected every 1 h of charge or discharge followed by 30 min of rest and at the end of charge or discharge. All the electrochemical measurements were performed on a Landt battery cycler or a BioLogic cycler. All experiments were conducted at room temperature (25 °C).

4.4 Scanning electron microscopy

The scanning electron microscopy (SEM) morphologies of the deposited Li were characterized with a Hitachi S4800 scanning electron microscope set at 3 kV.

4.5 Micro-computed tomography (μ-CT)

To prepare the μ-CT samples, anode-free cells were fabricated by loading 4 mg of fine LPSC powders into a PEEK tube with an inner diameter of 2 mm, followed by pressing into a pellet under low pressure. Afterwards, 1 mg of NMC cathode composites was loaded on one side of the SE pellet and compressed with a 2 mm diameter steel pillar by hand. The cell stack was then pressed at a high pressure of 350 MPa for 1 min to densify the two layers. A 2-mm diameter Ag-coated SS disc was placed on the other side of the SE pellet. The cell was sealed with two screws with O-rings and tightened to apply a stack pressure of around 15 MPa during cell testing. The cell was cycled at C/10 for 5 cycles.

The μ-CT scans of AFSSBs were collected at the Oak Ridge National Laboratory using a Zeiss Xradia Versa 520 system. X-rays with an energy of 60 kV (80 kV for higher resolution runs) were used for the scans. A 4× scintillator objective was used for the higher field-of-view (FOV) scans at 60 kV whereas a 20× scintillator objective was used for higher resolution and lower FOV scans. The μ-CT data were collected over a full 360° rotation of the sample (around the vertical axis) with 1601 evenly spaced projections. Voxel sizes of 1.07 μm and 0.76 μm were achieved with the 4× and 20× objectives, respectively. Raw data were reconstructed with the Zeiss reconstructor software. Image segmentation and 3D rendering creation were performed using DragonFly.

4.6 *Operando* neutron imaging

The *operando* neutron imaging was conducted on the Multimodal Advanced Radiography Station (MARS) HFIR beamline CG-1D, at Oak Ridge National Laboratory. The detector-to-pinhole distance was 6.59 m, and the pinhole diameter was 11 mm. The cells used for *operando* neutron imaging were fabricated by loading 15 mg of SE powders into a quartz tube with a diameter of 4 mm, followed by pressing into a pellet under a low pressure of 20 MPa. The cathode composite powder was then pressed onto one side of the SE pellet under a pressure of 350 MPa. A SS disk as the anode current collector and one piece of carbon felt with a diameter of 4 mm were

sequentially placed on the other side of the SE pellet. A carbon-coated aluminum foil disk was used as the cathode current collector. A stacking pressure of 7.5 MPa was applied to the cell by an aluminum framework during the cell testing. All gaps in the cell were further sealed using sealing grease and hot-melt glue. During the *operando* neutron imaging measurement, the cell was positioned in front of a scientific Complementary Metal–Oxide–Semiconductor (sCMOS) camera system (QHY600M and QHYCCD, Beijing, China) with a 20 μm thick Gd_2O_2S:Tb scintillator screen. Each image was acquired with an exposure time of 5 minutes under a neutron beam with a wavelength range of 0.8–6 Å and a peak flux of 2.2×10^6 n cm^{-2} s^{-1} at 2.6 Å. Open-beam and dark current reference images were acquired before and after *operando* imaging to normalize raw images. The ambient temperature during imaging was approximately 20 °C. Data processing was conducted using the ORNL-developed neutron imaging Jupyter Notebook[37] and Fiji image analysis software.[38]

Author contributions

H. Z. directed the project. H. Z. and J. W. designed the experiments. J. W. performed all the electrochemical characterization studies. Y. Z., J. T., C. X., and S. H. helped with *operando* neutron imaging measurements. C. X., Y. Z., J. W., and H. Z. analyzed the neutron imaging data. M. Y. helped with schematic drawing. X. Z. and E. C. helped with the micro-CT measurements. M. G. and K. S. B. helped with the Ag deposition. J. W. wrote the manuscript. All the authors contributed to the discussion of the manuscript.

Conflicts of interest

The authors declare no competing financial interests.

Data availability

The data that support the findings of this study are available from the corresponding author upon reasonable request. Correspondence and requests for materials should be addressed to H. Zhu.

The supporting information includes supplementary operando neutron imaging results, electrochemical characterization, surface morphology analysis, and in situ EIS/DRT analysis. Supplementary information (SI) is available. See DOI: https://doi.org/10.1039/d6eb00128a.

Acknowledgements

H. Z. acknowledges the financial support received from the Office of Science Department of Energy under Award Number DE-SC0024528. This work was partially supported by the Department of Energy's Bioenergy Technologies Office. This research used resources at the High Flux Isotope Reactor, a DOE Office of Science User Facility operated by the Oak Ridge National Laboratory. The beamtime was allocated to MARS (CG-1D), proposal number IPTS-32720. M. G. and K. S. B. acknowledge support from the National Science Foundation, under award number DMR-2310895.

References

1 D. H. S. Tan, A. Banerjee, Z. Chen and Y. S. Meng, From nanoscale interface characterization to sustainable energy storage using all-solid-state batteries, *Nat. Nanotechnol.*, 2020, **15**, 170–180, DOI: 10.1038/s41565-020-0657-x.

2 M. Burton, *et al.*, Techno-economic assessment of thin lithium metal anodes for solid-state batteries, *Nat. Energy*, 2024, **10**, 135–147, DOI: 10.1038/s41560-024-01676-7.

3 S. Xia, X. Wu, Z. Zhang, Y. Cui and W. Liu, Practical challenges and future perspectives of all-solid-state lithium-metal batteries, *Chem*, 2019, **5**, 753–785, DOI: 10.1016/j.chempr.2018.11.013.

4 H. Wan, Z. Wang, W. Zhang, X. He and C. Wang, Interface design for all-solid-state lithium batteries, *Nature*, 2023, **623**, 739–744, DOI: 10.1038/s41586-023-06653-w.

5 W. Z. Huang, *et al.*, Anode-free solid-state lithium batteries: A review, *Adv. Energy Mater.*, 2022, **12**, 2201044, DOI: 10.1002/aenm.202201044.

6 K. H. Kim, *et al.*, Near-strain-free anode architecture enabled by interfacial diffusion creep for initial-anode-free quasi-solid-state batteries, *Nat. Commun.*, 2024, **15**, 3586, DOI: 10.1038/s41467-024-48021-w.

7 J. Wang and H. Zhu, Sulfide-based anode-free solid-state batteries: Key challenges and emerging solutions, *ACS Energy Lett.*, 2025, **10**, 2377–2391, DOI: 10.1021/acsenergylett.5c00517.

8 Y. Qiao, *et al.*, A high-energy-density and long-life initial-anode-free lithium battery enabled by a Li_2O sacrificial agent, *Nat. Energy*, 2021, **6**, 653–662, DOI: 10.1038/s41560-021-00839-0.

9 S. E. Sandoval, *et al.*, Electro-chemo-mechanics of anode-free solid-state batteries, *Nat. Mater.*, 2025, **62**, 9370, DOI: 10.1038/s41563-024-02055-z.

10 T. Zhang, *et al.*, Loss and recovery of effective lithium in anode-free solid-state lithium metal batteries, *Adv. Mater.*, 2025, **37**, e05695, DOI: 10.1002/adma.202505695.

11 V. Pande and V. Viswanathan, Computational screening of current collectors for enabling anode-free lithium metal batteries, *ACS Energy Lett.*, 2019, **4**, 2952–2959, DOI: 10.1021/acsenergylett.9b02306.

12 J. Qian, *et al.*, Anode-free rechargeable lithium metal batteries, *Adv. Funct. Mater.*, 2016, **26**, 7094–7102, DOI: 10.1002/adfm.201602353.

13 J. Wang, *et al.*, Fundamental understanding of "fresh" lithium nucleation and growth in sulfide-based anode-free solid-state batteries: Effects of substrate, current density, and Li(+) supply, *Small*, 2025, e06473, DOI: 10.1002/smll.202506473.

14 D. S. Ko, *et al.*, Mechanism of stable lithium plating and stripping in a metal-interlayer-inserted anode-less solid-state lithium metal battery, *Nat. Commun.*, 2025, **16**, 1066, DOI: 10.1038/s41467-025-55821-1.
15 D. Cao, *et al.*, Enhancing lithium stripping efficiency in anode-free solid-state batteries through self-regulated internal pressure, *Nano Lett.*, 2023, **23**, 9392–9398, DOI: 10.1021/acs.nanolett.3c02713.
16 S. H. Park, K. G. Naik, B. S. Vishnugopi, P. P. Mukherjee and K. B. Hatzell, Lithium kinetics in Ag–C porous interlayer in reservoir-free solid-state batteries, *Adv. Energy Mater.*, 2024, **15**, 2405129, DOI: 10.1002/aenm.202405129.
17 D. Spencer-Jolly, *et al.*, Structural changes in the silver–carbon composite anode interlayer of solid-state batteries, *Joule*, 2023, **7**, 503–514, DOI: 10.1016/j.joule.2023.02.001.
18 Y.-G. Lee, *et al.*, High-energy long-cycling all-solid-state lithium metal batteries enabled by silver–carbon composite anodes, *Nat. Energy*, 2020, **5**, 299–308, DOI: 10.1038/s41560-020-0575-z.
19 Y. Huang, *et al.*, Hydride-based interlayer for solid-state anode-free battery, *ACS Energy Lett.*, 2024, **9**, 3409–3417, DOI: 10.1021/acsenergylett.4c00704.
20 Y. Sohn, *et al.*, Dual-seed strategy for high-performance anode-less all-solid-state batteries, *Adv. Mater.*, 2024, **36**, e2407443, DOI: 10.1002/adma.202407443.
21 Y. Wang, *et al.*, Control of two solid electrolyte interphases at the negative electrode of an anode-free all solid-state battery based on argyrodite electrolyte, *Adv. Mater.*, 2025, **37**, e2410948, DOI: 10.1002/adma.202410948.
22 J. Oh, Y. Sohn and J. W. Choi, High-performance anode-less all-solid-state batteries enabled by multisite nucleation and an elastic network, *EES Batteries*, 2025, **1**, 566–575, DOI: 10.1039/d5eb00050e.
23 J. Oh, *et al.*, Lithio-amphiphilic nanobilayer for high energy density anode-less all-solid-state batteries operating under low stack pressure, *Energy Environ. Sci.*, 2024, **17**, 7932–7943, DOI: 10.1039/d4ee03130j.
24 J. H. Lee, *et al.*, Interfacial stabilization strategy via In-doped Ag metal coating enables a high cycle life of anode-free solid-state Li batteries, *Energy Storage Mater.*, 2024, **69**, 103398, DOI: 10.1016/j.ensm.2024.103398.
25 J. Oh, *et al.*, Kinetically engineered lithiophilic dual-metal layers for dendrite-free, high-energy anode-less all-solid-state batteries, *Battery Energy*, 2025, **4**, e70038, DOI: 10.1002/bte2.20250035.
26 D. Cao, *et al.*, Li Dynamics in mixed ionic-electronic conducting interlayer of all-solid-state Li-metal batteries, *Nano Lett.*, 2024, **24**, 1544–1552, DOI: 10.1021/acs.nanolett.3c04072.
27 T. Ji, *et al.*, Operando neutron imaging-guided gradient design of Li-ion solid conductor for high-mass-loading cathodes, *Nat. Commun.*, 2025, **16**, 7667, DOI: 10.1038/s41467-025-62518-y.
28 Y. Wang, *et al.*, Mechanical milling – Induced microstructure changes in argyrodite LPSCl solid-state electrolyte critically affect electrochemical stability, *Adv. Energy Mater.*, 2024, **14**, 2304530, DOI: 10.1002/aenm.202304530.
29 Y. Wang, *et al.*, Stable anode-free all-solid-state lithium battery through tuned metal wetting on the copper current collector, *Adv. Mater.*, 2023, **35**, e2206762, DOI: 10.1002/adma.202206762.
30 J. Lee, *et al.*, Room-temperature anode-less all-solid-state batteries via the conversion reaction of metal fluorides, *Adv. Mater.*, 2022, **34**, e2203580, DOI: 10.1002/adma.202203580.
31 J. Kim, *et al.*, Regulating Li electrodeposition by constructing Cu–Sn nanotube thin layer for reliable and robust anode-free all-solid-state batteries, *Carbon Energy*, 2024, **6**, e610, DOI: 10.1002/cey2.610.
32 D. B. Seo, *et al.*, Tailoring artificial solid electrolyte interphase via MoS(2) sacrificial thin film for Li-free all-solid-state batteries, *Nano-Micro Lett.*, 2025, **17**, 224, DOI: 10.1007/s40820-025-01729-w.
33 L. Lin, *et al.*, Tailoring Li deposition by regulating structural connectivity of electrochemical Li reservoir in Li-metal batteries, *Angew. Chem.*, 2024, **63**, e202319847, DOI: 10.1002/anie.202319847.
34 Y. Xiao, *et al.*, The regulation of lithium plating behavior by state of stripping in working lithium metal anode, *Adv. Energy Mater.*, 2023, **13**, 2300959, DOI: 10.1002/aenm.202300959.
35 J.-A. Lee, *et al.*, Unveiling degradation mechanisms of anode-free Li-metal batteries, *Energy Storage Mater.*, 2024, **73**, 103826, DOI: 10.1016/j.ensm.2024.103826.
36 X. Sun, *et al.*, All-solid-state Li–S batteries enhanced by interface stabilization and reaction kinetics promotion through 2D transition metal sulfides, *Adv. Mater. Interfaces*, 2022, **9**, 2200539, DOI: 10.1002/admi.202200539.
37 J.-C. Bilheux, H. Bilheux, J. Lin, I. Lumsden and Y. Zhang, Neutron imaging analysis using jupyter Python notebook, *J. Phys. Commun.*, 2019, **3**, 083001, DOI: 10.1088/2399-6528/ab3bea.
38 J. Schindelin, *et al.*, Fiji: An open-source platform for biological-image analysis, *Nat. Methods*, 2012, **9**, 676–682, DOI: 10.1038/nmeth.2019.